A Petascale Nonhydrostatic Atmospheric Dynamical-Core
in the HOMME Framework
Final Report

1. Overview

The High-Order Method Modeling Environment (HOMME) is a framework for building scalable, conservative atmospheric models for climate simulation and general atmospheric-modeling applications. Its spatial discretizations are based on Spectral-Element (SE) and Discontinuous Galerkin (DG) methods. These are local methods employing high-order accurate spectral basis-functions that have been shown to perform well on massively parallel supercomputers at any resolution and scale particularly well at high resolutions. HOMME provides the framework upon which the CAM-SE community atmosphere model dynamical-core is constructed. In its current incarnation, CAM-SE employs the hydrostatic primitive-equations (PE) of motion, which limits its resolution to simulations coarser than 0.1° per grid cell. The primary objective of this project is to remove this resolution limitation by providing HOMME with the capabilities needed to build nonhydrostatic models that solve the compressible Euler/Navier-Stokes equations.

To achieve this goal, we have been pursing two complimentary efforts: development of a Discontinuous-Galerkin Nonhydrostatic (DG-NH) model and a Spectral-Element Nonhydrostatic (SE-NH) model. The SE-NH effort is intended to be incremental, retaining as many features of the current CAM-SE formulation as possible, thereby reducing its development time and facilitating its adoption. The DG-NH model is a more comprehensive effort that replaces both the horizontal and vertical discretizations with a high-order Discontinuous-Galerkin representation and generalizes the vertical coordinates.

The DG-NH model has progressed this year through the completion of an x-z limited-area model and the technologies developed therein. Terrain-following z-coordinates, vertical DG operators, and an atmospheric sponge-layer have been developed. The model performs well on a standard set of two-dimensional benchmarks including the rising bubble, density current, and orographic-wave tests. Porting of these capabilities to the HOMME DG-3d code is ongoing. An HE-VI split explicit time-stepping scheme was implemented and applied to both the shallow-water equations and the x-z DG-NH model. This enables a much larger time-step in the solution of the compressible Euler equations, overcoming the strict vertical CFL limit. Performance of the HOMME DG 3d code was enhanced by 10% by customizing the data transfer routines to eliminate corner elements (required only for SE simulations) and by the use of improved communication-overlapping and asynchronous MPI calls. A fully implicit version of the DG-3d code was also implemented, which greatly accelerates performance at lower resolutions where communication bandwidth is less important.

The SE-NH model is designed to solve the 3d compressible-Euler equations in hybrid terrain-following pressure coordinates, based on the model of Laprise [1]. To date, coding of this model has been completed, and a comprehensive test suite has been developed for its evaluation based upon the DCMIP Dynamical-Core Model Intercomparison Project [2]. These tests range from simple transport, to dry rotating atmospheres, and finally to moist dynamics. While the Laprise model performed well on most tests, a subset exhibited numerical instability. As discussed by Thurburn 2005 [3], development of a stable compressible-Euler formulation is challenging, requiring a careful choice of prognostic variables, boundary conditions, and vertical variable staggering, where most combinations are unstable. With this in mind, the SE-NH model was split into multiple variants that sample this parameter space. Several of the alternative formulations show much greater stability than the original. After intercomparison of the models, we will choose the model or models with the greatest stability and accuracy. Additionally, new capabilities have been developed in HOMME which enable vertical spectral-element discretizations of both the primtive-equation and nonhydrostatic models which is important for increasing speed and accuracy in high resolution simulations.

2. The Discontinuous Galerkin Nonhydrostatic Model (DG-NH)

The DG-NH effort is aimed at developing a model using Discontinuous Galerkin discretizations in both the horizontal and vertical directions, and terrain-following z coordinates in the vertical. The DG method was chosen as it often produces higher quality results than the SE method, and it is more scalable with less intra-element communication. The z coordinate was chosen as it is employed in multiple successful nonhydrostatic models, and we believe it has the potential for greater accuracy, as it is free from time-dependent terrain metrics [4].

2.1. The DG-NH Limited-Area Model

Use of the 2-dimensional DG-NH x-z model enables the development of nonhydrostatic technologies more rapidly, in a limited domain of very high resolution, that would be computationally prohibitive on the full sphere. It is also much simpler than the fully dynamical-core, facilitating rapid code re-design. As features are finalized, they are ported to the full HOMME-DG branch. With this approach, we have developed the tools necessary to implement the horizontal DG and vertical DG operators, a horizontal LDG diffusion mechanism, a terrain-following z coordinate system, as well as implicit and split-explicit time-stepping schemes.

2.2. DG-NH Governing Equations

Total mass and energy conservation is extremely important for climate scale integration, therefore a flux-form compressible Navier-Stoke system is employed, which is inherently conservative. The density and pressure are split into hydrostatic and nonhydrostatic components $\rho = \bar{\rho} + \rho'$ and $p = \bar{p} + p'$, where the mean values $\bar{\rho}$ and $\bar{p}$ are in hydrostatic balance $\frac{\partial \bar{p}}{\partial z} = -\bar{\rho} g$. The governing equations are

$$\frac{\partial \rho}{\partial t} + \nabla \cdot (\rho \boldsymbol{V}) = 0 \tag{1}$$

$$\frac{\partial \rho \boldsymbol{V}}{\partial t} + \nabla \cdot (\rho \boldsymbol{V} \otimes \boldsymbol{V}) = -\nabla p' - \rho' g \hat{\boldsymbol{k}} - 2\rho \boldsymbol{\Omega} \times \boldsymbol{V} + \boldsymbol{F}_M \tag{2}$$

$$\frac{\partial \rho \theta}{\partial t} + \nabla \cdot (\rho \theta \boldsymbol{V}) = 0 \tag{3}$$

$$\frac{\rho q_k}{\partial t} + \nabla \cdot (\rho q_k \boldsymbol{V}) = 0 \tag{4}$$

where $(2\rho\boldsymbol{\Omega} \times \boldsymbol{V})$ is the Coriolis force, $\boldsymbol{F}_M$ is the forcing term including the diffusive fluxes, $\boldsymbol{\Omega}$ is Earth's angular velocity, and $\hat{\boldsymbol{k}}$ is the radial unit vector. The Coriolis term is neglected in the 2D x-z model.

2.3. Terrain following coordinates and boundary conditions

Accurate representation of the terrain is very important for nonhydrostatic modeling where mountain lee-waves are forced by the topography of the Earth's surface. Although the DG method is capable of handling complex domains [5], we prefer to use the classical terrain-following height coordinates introduced by Gal-Chen and Somerville [6]. If $h = h(x)$ is the prescribed mountain profile and z_T is the top of the model domain, as shown in Figure 1, then the vertical z height coordinate can be transformed to the monotonic ζ coordinate using the following mapping:

$$\zeta = z_t \frac{z - h(x)}{z_T - h(x)}, \qquad z(\zeta) = h(x) + \zeta \frac{(z_t - h)}{z_T}; \qquad h(x) \le z \le z_T \tag{5}$$

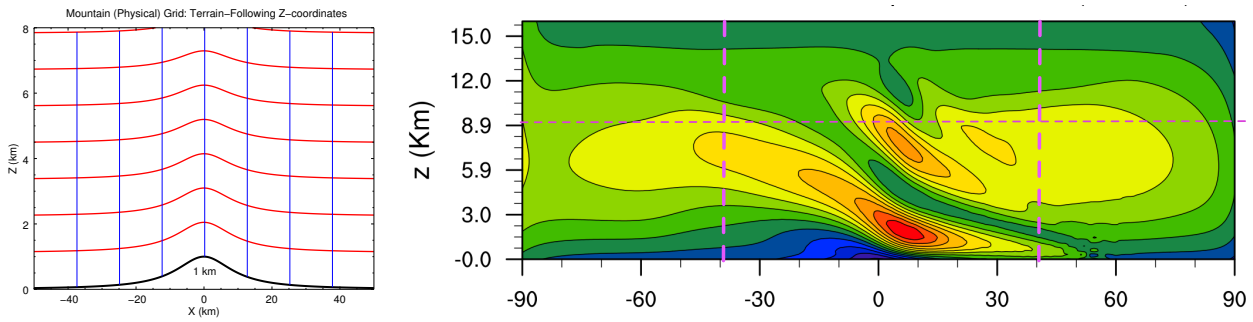

Figure 1: Left: Terrain-following z coordinates in physical domain. Right: Orographic-wave test on the computational grid with sponge layers indicated by dashed lines

Sponge-layers are employed on the sides and top of the x-z model to implement non-reflective boundary conditions wherein prognostic variables are relaxed to their basic state. For example the top-boundary

velocity condition is

$$\frac{\partial \boldsymbol{V}}{\partial t} = ... - \tau(x,z)(\boldsymbol{V} - \boldsymbol{V}_0), \qquad \tau(x,z) = \begin{cases} 0, & \text{if} z < z_D \\ \tau_0 \frac{z - z_D}{z_T - z_D}^4, & \text{otherwise} \end{cases} \tag{6}$$

2.4. NH-DG testing

A series of standard benchmarks has been implemented and applied to the DG-NH limited area model to validate its accuracy and performance. These tests include the the warm convective bubble, an interia-gravity wave (IGW) test, the Straka density-current test, and an orographic-wave test (flow over an isolated mountain).

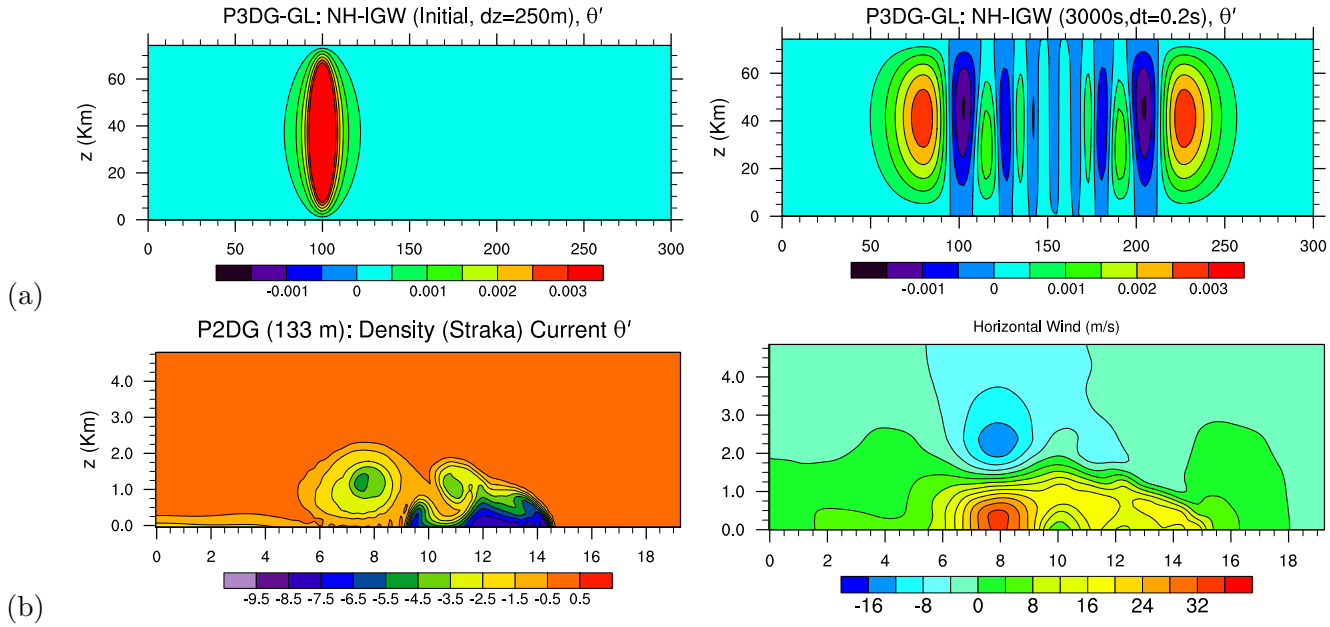

Figure 2: Tests of the x-z DGNH model (a) Potential temperature perturbations θ' in inertial-gravity wave test (b) Straka density-current test at a resolution $\Delta\bar{z} = 100$ m using the explicit SSP-RK time stepping and a time step of $\Delta t = 0.04$s

The nonhydrostatic inertia-gravity wave (IGW) test shown in figure 2(a) introduced by Skamarock and Klemp [7] serves as a useful tool to check the accuracy of various time-stepping schemes used for NH dynamics. This test examines the evolution of a potential temperature perturbation θ', in a channel with periodic boundary conditions on the left and right boundaries. The initial perturbation radiates to the left and right symmetrically, while being advected to right with a prescribed mean horizontal flow.

The density current benchmark introduced by Straka et al. [8] and shown in figure 2(b) is often used to evaluate numerical schemes developed for atmospheric models. The Straka density current mimics cold outflow from a convective system and tests a model's ability to control oscillations when numerical viscosity is applied. This test involves evolution of a density flow generated by a cold bubble in a neutrally stratified atmosphere. The cold bubble descends to the ground and spreads out in the horizontal direction, forming three Kelvin-Helmholtz shear instability rotors along the cold front surface. This is a test-case suitable for testing the LDG diffusion option in the DG-NH model.

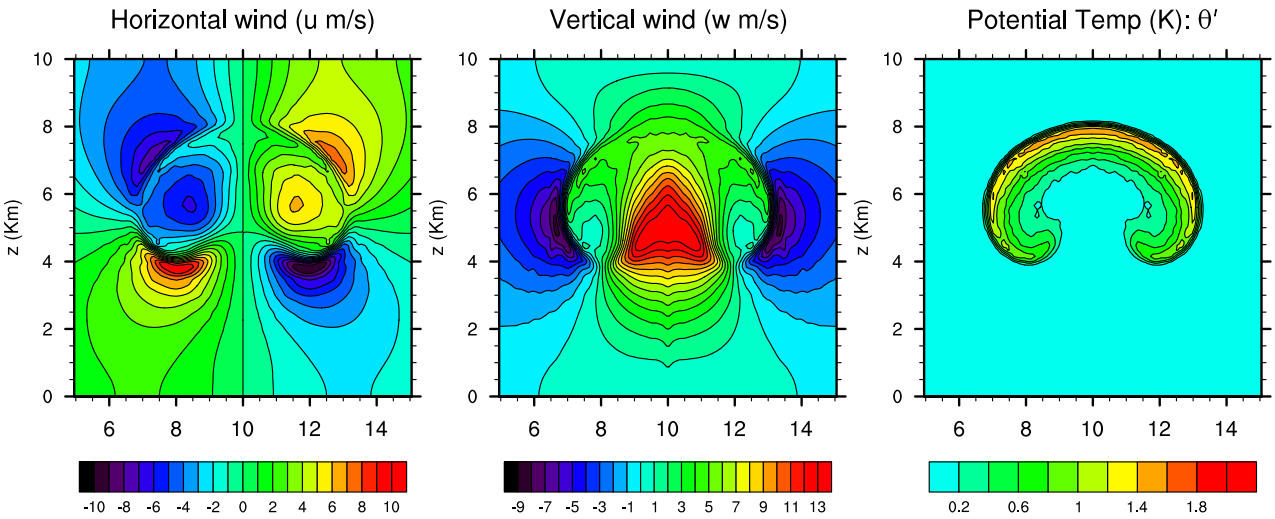

Figure 3: Tests of the x-z DGNH model Connvective bubble at 125m resolution at 1000s: horizontal wind u and vertical wind v in m/s and potential temperature deviation θ' in Kelvin.

The convective bubble test shown in figure 3 embodies a phenomenon of great interest to mesoscale type flows, and is widely used to validate the ability of numerical models for simulating the atmospheric motions due to thermodynamic effects [42]. The thermal bubble is warmer than the ambient air and thus it rises while deforming as a result of the shearing motion caused by the velocity field gradients until it forms into the shape of a mushroom cloud.

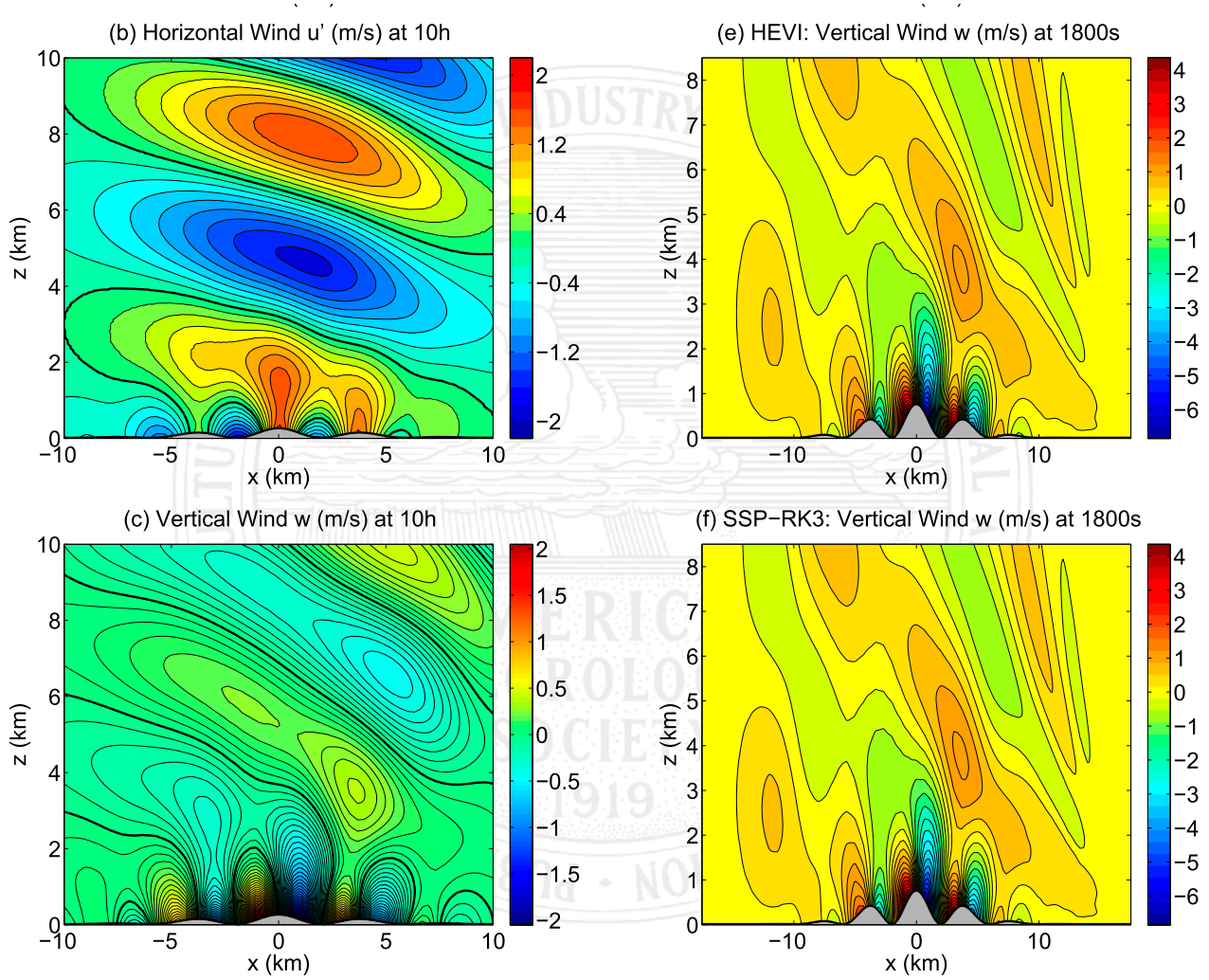

Figure 4: Test of the HEVI time-integration scheme in the x-z DGNH limited area model. (b) horizontal wind field perturbation for Schär mountain range of height $h_0 = 250$ m. (c) Vertical wind field w. (e) Vertical wind field for $h_0 = 750$ m mountain range for the HEVI scheme (f) Vertical wind field for the SSP-RK3 scheme.

A Schär mountain test was implemented to evaluate the performance of the HEVI scheme in handling complex topography. The Schär mountain test simulates the generation of gravity waves by a constant horizontal flow field in a uniform stratified atmosphere impinging on a nonuniform mountain range. As demonstrated in fig. 4, no visually distinguishable difference is observed between the results of the SSP-RK3 and HEVI time integration schemes. There is no unphysical distorted wave pattern shown in the upper level of the domain and our results are comparable to other publications.

2.5. Implicit Time Integration

The standard solver for the DG-NH model is the SSP-RK3, three-stage strong-stability preserving Runge-Kutta explicit solver. In addition we have developed a fully implicit solver and a horizontally-explicit, vertically-implicit HE-VI solver. The fully implicit solver enables large time-steps to be taken in low resolution simulations where global communication is not the limiting factor. The HE-VI solver enables the nonhydrostatic model to overcome the strict vertical CFL condition and its extreme time constraint, and is useful for simulations at all resolutions. For the implicit components of both solvers, we employ the Diagonally Implicit Runge-Kitta (DIRK) method [9] together with a Jacobian-free Netwon Krylov solver, as it enables us to solve the non-linear systems individually. The DIRK method requires the solution of several non-linear equations $F(U) = 0$, using Newton's method.

$$U^{s+1} = U^s - DF(U^s)^{-1} DF(u^s) \quad \text{with } s \geq 0$$

where DF denotes the Jacobian of the system evaluated at u^s. This requires a solution of a linear system of the form

$$DF(U^s)p = F(U^s)$$

for each Newton iteration s. Since the computation of the Jacobian is complicated and memory intensive, it is approximated by

$$DF(U^s)p \approx \frac{1}{\varepsilon}(F(u + \varepsilon p) - F(u))$$

The choice of the parameter ε is an important consideration as discussed in Knoll & Keyes [10]. Our choice is

$$\varepsilon := \begin{cases} \sqrt{(1 + ||U||)\varepsilon_m} & \text{if } ||p||^2 > \varepsilon_m \\ \epsilon_m & \text{otherwise} \end{cases}$$

where $\varepsilon_m \approx 10^{-15}$ denotes machine precision. The resulting linear system is solved with a GMRES iteration. For our applications usually the number of newton iterations is very small. Therefore, the performance of the HE-VI solver is closely related to the number of iterations of the linear GMRES solver. This can be reduced by a proper preconditioning which is a topic of ongoing research.

2.6. HE-VI Time Integration

Fast acoustic waves are a significant challenge for nonhydrostatic solvers. Since the vertical grid spacing is typically much smaller than the horizontal grid spacing in climate models, the vertical CFL condition requires unacceptable small time-steps when using a fully explicit time-integration scheme. Employing an implicit solver in the vertical enables us to overcome this limitation without having to modify the underlying partial differential equations. An implicit treatment in the vertical direction does not require any intra-node communication as each column is maintained on a single node. Therefore, we expect the excellent scaling behavior on up to $\mathcal{O}(10^5)$ processors will be maintained.

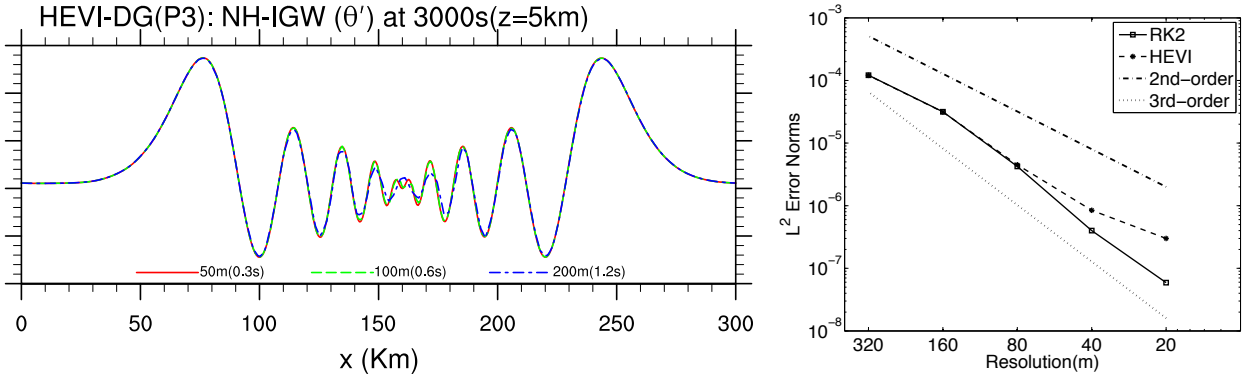

Figure 5: The left panel shows the profiles of potential temperature perturbation θ'(K) for the inertia gravity-wave test at z = 5 km, at various resolution for HEVI-DG simulations. Convergence of a second order DG-NH model is shown on the right panel for IGW tests with both HEVI and explicit RK-DG time integrators.

Our HE-VI solver uses Strang-type operator splitting which permits $\mathcal{O}(\Delta t^2)$ accurate time stepping. The Euler system for $\boldsymbol{U} = (\rho', \rho u, \rho w, (\rho\theta)')^T$ is split into horizontal (x) and vertical (z) directions in the following way

$$\text{full system} \quad \frac{\partial \boldsymbol{U}}{\partial t} + \frac{\partial \boldsymbol{F}^x}{\partial x} + \frac{\partial \boldsymbol{F}^z}{\partial z} = \boldsymbol{S}(\boldsymbol{U}) \tag{7}$$

$$\text{H-part} \quad \frac{\partial \boldsymbol{U}}{\partial t} + \frac{\partial \boldsymbol{F}^x}{\partial x} = \boldsymbol{S}^x(\boldsymbol{U}) = 0 \tag{8}$$

$$\text{V-part} \quad \frac{\partial \boldsymbol{U}}{\partial t} + \frac{\partial \boldsymbol{F}^z}{\partial z} = \boldsymbol{S}^z(\boldsymbol{U}) = (0, 0, -\rho' g, 0)^T \tag{9}$$

We apply an H-V-H splitting approach to solve this system, where the the horizontal explicit stage is applied twice with timestep $\Delta t/2$ and the vertical system is solved implicitly once with timestep Δt. When using an implicit method for the vertical direction we observe that the CFL condition can be relaxed to the CFL condition for the horizontal part. However, the necessity of solving an implicit system introduces additional computational expense, and reducing this cost is an ongoing area of research.

Figure 5 shows the convergence of HEVI-DG at various resolutions for the IGW test. We sample θ' (K) along a line at $z = 5$ km, with the vertical resolutions $\Delta\bar{x} = 200$, 100, 50 m, as shown on the left panel of Figure 5. The distribution is symmetric with respect to the midpoint ($x = 16$ km), and captures fine features of the IGW as the resolution increases. This result is consistent with those reported in [5], where a high-order DG model was used. The h-convergence of the DG-NH model is demonstrated in the right panel of Figure 5. The convergence rate is plotted for HEVI-DG as well as RK-DG by halving the vertical resolution $\Delta\bar{x} = 320$, ..., 20 m. The convergence rate, which is very similar for both time-stepping methods, lies between second and third-order as expected for a three point DG method.

2.7. Performance Enhancements

To improve the performance of HOMME-DG we have revised the communication implementation in the HOMME framework. The connectivity is reduced for DG simulations. We have improved communication overlap with computations, and asynchronous MPI operations are permitted. In the algorithm below we outline the *packAndSend* routine and the *receiveAndUnpack* routine. Both routines overlap the work done by send/receive with the corresponding pack/unpack work. As both routines are called separately it is also possible to place some computation work in between the call packAndSend and receiveAndUnpack. This, however, requires some algorithmic restructuring which is not always easy or possible. For that reason our implementation provides at least the more simple overlap of pack/unpack with communication calls.

To implement the overlap of pack/unpack routines with the communication itself we generated the following mapping. $l \in \mathcal{L}_p$ are all processes that one process p needs to communicate with. Using this set we generate a set that contains all elements $e \in \mathcal{E}_l$ that are linked to process l, either the edge or the vertices.

```
packAndSend:
  for l ∈ L_p do
  |  for e ∈ E_l do
  |  |  packData( e, l )
  |  end
  |  send data in message buffer
  |  MPI_Isend( l )
  end
  for l ∈ L_p do
  |  post corresponding receives
  |  MPI_Irecv( l )
  end
```

```
receiveAndUnpack:
  for l ∈ L_p do
  |  r_l ← 0
  end
  for l ∈ L_p do
  |  if r_l = 0 then
  |  |  test whether message
  |  |  was completely received
  |  |  r_l ← MPI_test( l )
  |  |  if r_l = 1 then
  |  |  |  forall the e ∈ E_l do
  |  |  |  |  unpackData( e, l )
  |  |  |  end
  |  |  end
  |  end
  end
```

In Figure 6 we present the strong scaling of the DG code for the Jablonowski-Williamson test case. The revised version using reduced connectivity and the overlapping techniques results in better performance. The computation time is reduced by 10%, referred to as non-blocking in Figure 6. The strong scaling of the non-blocking version is very good up to 16 224 cores. The run on 16 224 cores, which for ne = 52 results in 1 element per core, still shows good strong scaling efficiency of 73% as compared to the run on 256 cores. For the blocking version we only get a strong scaling efficiency of 58% on 16224 cores when compared with 256 cores. Although at this high core count the number of elements per core is small and therefore not much work to overlap with the communication is left the non-blocking still exhibits a significant improvement.

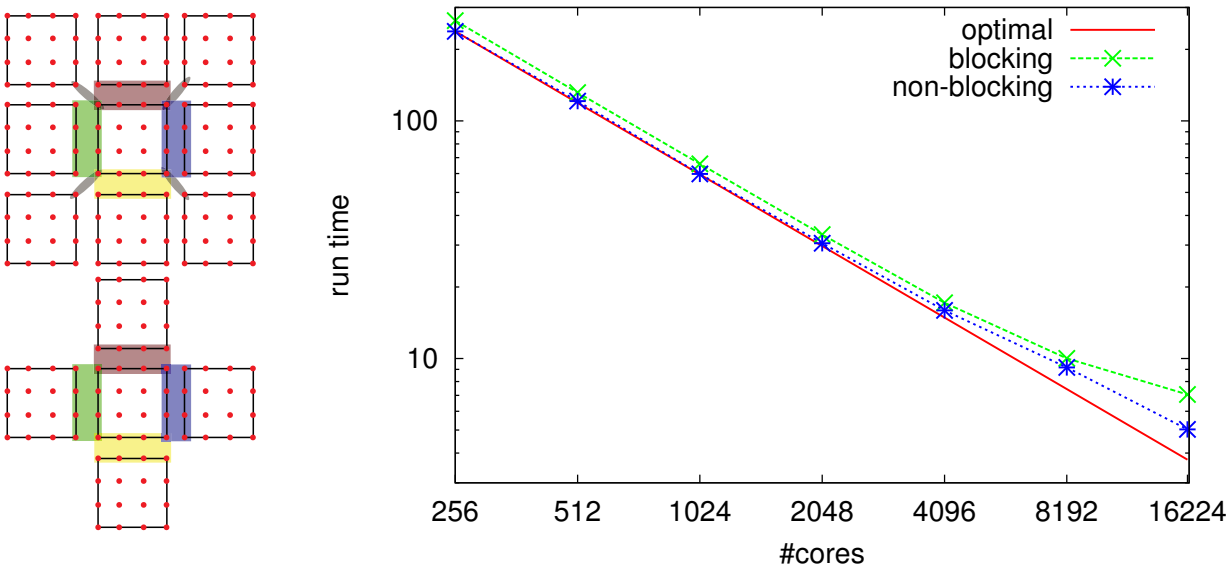

Figure 6: Performance improvements: (left) Performance is improved in DG simulations by removing the corner elements required by SE simulations. (right) Strong scaling of HOMME-DG for the Jablonowski-Williamson baroclinic wave instability test case with NP = 6 and ne = 52 shows the performance improvement due to overlapping, non-blocking communication.

3. The Spectral-Element Nonhydrostatic Model (SE-NH)

In contrast with the DG-NH model already described, the SE-NH effort represents an attempt to create a nonhydrostatic model that is as closely related to the existing CAM-SE formulation as possible. This allows us to reuse most of the existing dynamical-core code, and should make it easier to integrate a nonhydrostatic model into the CAM framework. Like CAM-SE, this model employs a hybrid-terrain following pressure vertical coordinate η which is defined implicitly by the equation for hydrostatic pressure $\pi = A(\eta)\pi_o + B(\eta)p_s$. The vertical discretization method is a second-order mimetic finite-differencing scheme. The governing equations, first formulated by Laprise [1], are

$$\frac{d\boldsymbol{u}}{dt} = -f\hat{\boldsymbol{k}}\times\boldsymbol{u} - \frac{RT}{p}\nabla_\eta p - \left(1 + \frac{\partial p'}{\partial \pi}\right)\nabla_\eta \Phi \tag{10}$$

$$\frac{dT}{dt} = \frac{RT}{c_p p}\left(\dot{\pi} + \dot{p}'\right) + \frac{Q}{c_p} \tag{11}$$

$$\frac{\partial \pi_s}{\partial t} = \int_1^{\eta_{\text{top}}} \nabla_\eta \cdot \left(\boldsymbol{u}\frac{\partial \pi}{\partial \eta}\right) d\eta \tag{12}$$

$$\frac{dw}{dt} = g\left(\frac{\partial p'}{\partial \pi}\right) \tag{13}$$

$$\frac{dp'}{dt} = -\dot{\pi} - p\frac{c_p}{c_v}\left(\nabla \cdot \boldsymbol{v}\right) + p\frac{Q}{c_v T} \tag{14}$$

where $\boldsymbol{f} = 2\Omega\cos(\phi)$ is the Coriolis parameter, $\Phi = gz$ is the geopotential height in η coordinates, p is the total pressure, π is the hydrostatic pressure component, and p' is the nonhydrostatic pressure component. This equation set reduces smoothly to the primitive equations used in CAM-SE when one neglects the nonhydrostatic pressure $\frac{dp'}{dt} = 0$, $p' = 0$ and the vertical acceleration term $\frac{dw}{dt} = 0$.

3.1. DCMIP tests

Unlike the limited area model, the NH-SE model is formulated globally, and simulations at nonhydrostatic resolutions of 10 km per grid-cell or higher are extraordinarily expensive and time-consuming to perform. However, nonhydrostatic effects can be induced at reasonable costs by employing a "shrunken planet" simulation were the radius of the earth is reduced by a factor of 10, 100, or 1000. The Dynamical Core Model Intercomparison Project (DCMIP) [2] tests were designed for this purpose, and we have adopted them to validate our model.

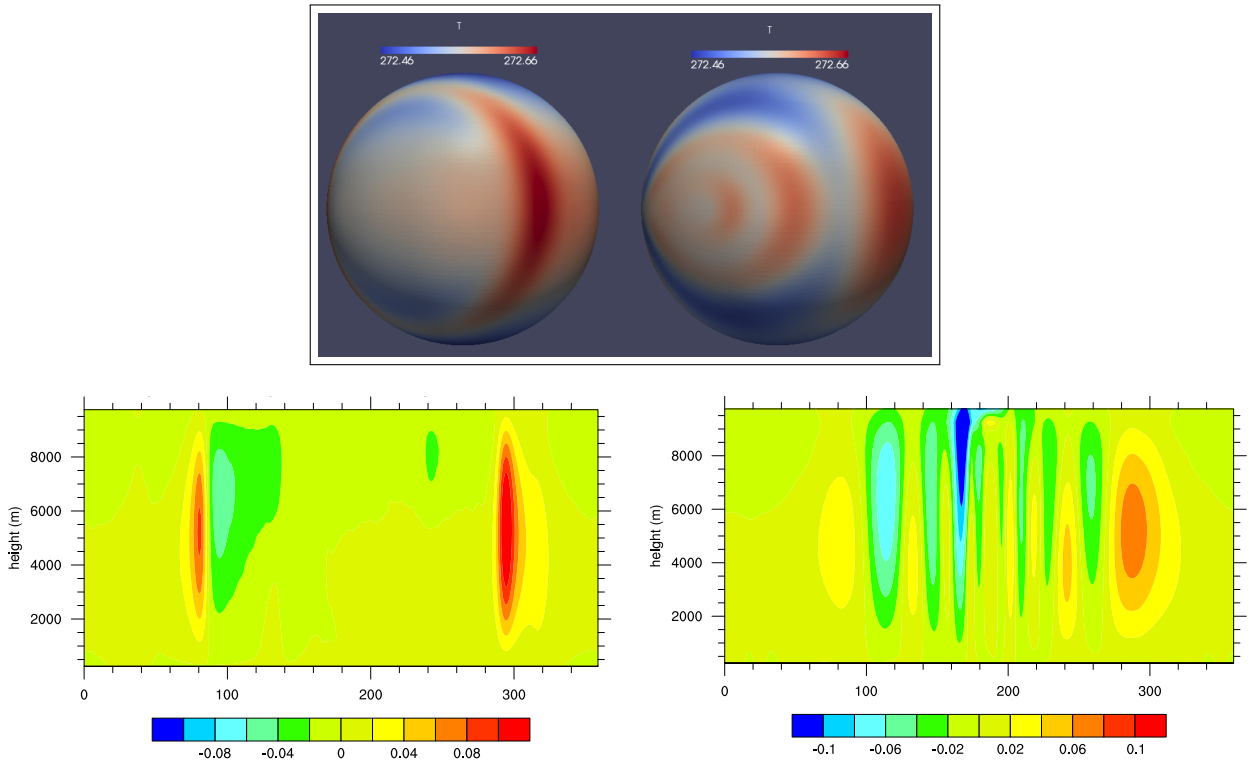

Figure 7: The DCMIP 3-1: Gravity wave test on a reduced planet at $t = 3000s$. (top) Temperature field comparison of the primitive equation solver on the left and the Laprise-NH model on the right. (bottom) Cross sections cut through the equator show that the PE model produces a single large pulse that differs significantly from the inertial oscillations produced by the NH model.

The dcmip 3-1 non-hydrostatic gravity-wave test in figure 7 examines the response of the NH-SE model to short time-scale wave motion triggered by a localized thermal perturbation of 1° K. When performed with a planetary radius reduced by a factor of $X = 125$, the gravity wave test discriminates clearly between hydrostatic and non-hydrostatic responses. The PE model on the left produces a single intense pulse, while the nonhydrostatic model produces a series of inertial oscillations. Results produced by the NH-SE model are quite similar to those of the ICON-IAP[11] and EndGame[12] models.

The traditional Polvani-Scott-Thomas baroclinic instability test was applied to both the Laprise model and the primitive equations as show inf figure 8. On an unscaled Earth, the NH model produces results that are virtually identical to the PE model, as expected. This is an important test, as the nonhydrostatic model should reduce smoothly to the hydrostatic model at coarse resolutions. The DCMIP 4-1-x test similarly examine an unstable jet of air that produces a baroclinic instability over time, but on a planet shrunken by a factor of X =10, 100, or 1000. At $X = 1000$ the onset of instability is delayed in the nonhydrostatic model relative to the PE model. These results match those of the EndGAME nonhydrostatic model precisely.

The DCMIP 2 tests examine nonhydrostatic effects of orography. Test 2-0 examines a steady-state atmosphere which evaluates the balance between the horizontal pressure-gradient term and the geopotential-gradient which arises in pressure-type coordinate due to their non-constant level height. Tests 2-1 and 2-2 examine the production of orographic waves with and without shear. Results for test 2-1 are shown in figure 9. The orographic waves produced in this test match those predicted by the other nonhydrostatic models very well, however we found the Laprise equations to exhibit instability in this test at later times. Somewhat surprisingly, this numerical instability was even more pronounced in the 'steady state' test 2-0, as the lack of flow-induced an mixing enables numerical modes to grow rapidly, if they exist. Therefore the DCMIP2-0 test is the first test we have applied to our new models as discussed below.

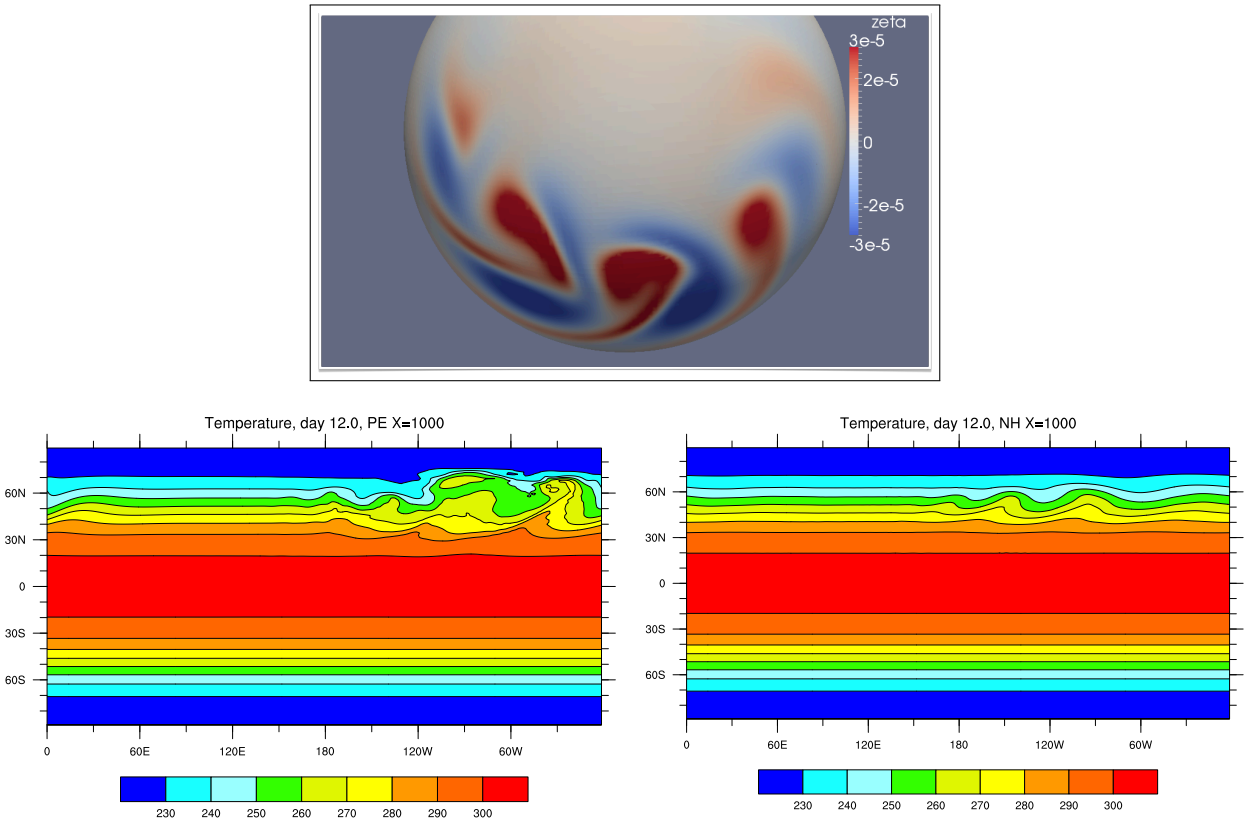

Figure 8: (top) Vorticity field produced by both the PE and NH equations are identical on the full sized planet at hydrostatic scales. (bottom) DCMIP test 4-1-3: Baroclinic instability on a reduced planet or radius $a/1000$. The nonhydrostatic Laprise results on the right show a delayed onset of the baroclinic instability relative to the primitive equations on the left.

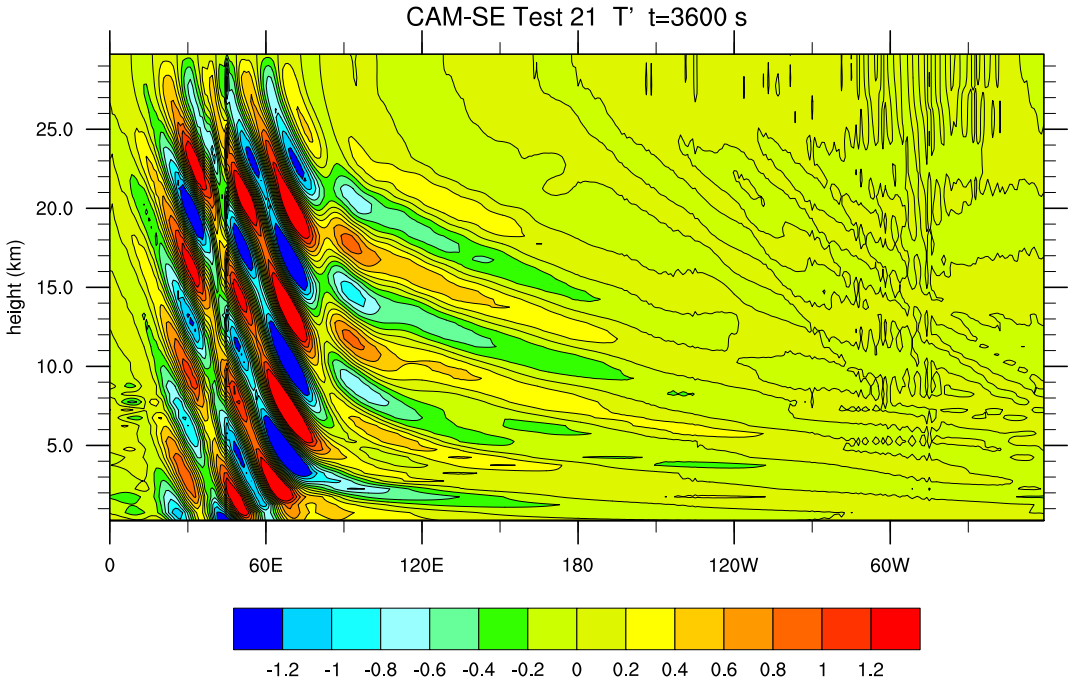

Figure 9: DCMIP Test 2-1: Orographic waves. Temperature perturbations are shown for flow a small mountain range.

3.2. Alternate Euler-Equation Formulations

Although the results of the DCMIP test produced by the Laprise model are very promising, several tests exhibited numerical instability. Although unfortunate, this is not unexpected, as similar difficulties have been reported by other groups developing pressure-based nonhydrostatic models, such as the ALADIN-NH

model used in the operational AROME weather prediction code [13]. The key to eliminating this numerical instability is to exchange prognostic variables, to adopt an alternative vertical staggering, or both. These issue were studied in great detail by Thurburn [3], who found that very few combinations are numerically stable. Therefore, we have begun developing alternative formulations of the Laprise equations, that use potential temperature θ and a $(w\theta, uvp)$ grid staggering. Initial results show the stability of these models to be much improved, and further testing is in progress.

3.3. Spectral-Element Vertical Coordinates

The accuracy of the nonhydrostatic solution can be improved through the use of a high-order spectral-element discretization in the vertical, rather than the low-order finite differences currently in place. Therefore, we have constructed spectral-element version of the primitive-equation solver, the Laprise model, and the alternative Euler models described above that enable us to examine the impact of high-order coordinates on the accuracy, speed, and scalability of the solvers. Initial results show excellent performance on the primitive-equation solver, and improved accuracy on the nonhydrostatic solvers but with a more restrictive timestep for purely explicit time integration. Stability properties of the Laprise and alternative Euler formulations seem to be similar to those of the finite-difference models.

3.4. Multi-model Framework

To speed the development and intercomparison of alternative nonhydrostatic models, we have implemented a multi-model framework that modularizes all of the components needed to implement a new model including: generalized vertical solvers, generalized DCMIP initial conditions, hyperviscosity, data i/o, and parallel edge-data communication. Using this new framework, we have implemented a series of new models with various vertical discretizations (finite-differences, spectral, spectral-elements) and various prognostic variables (prognostic T and θ for example) for the purposed of intercomparison. For each, we have constructed custom horizontal hyperviscosity routines and have explored multiple vertical diffusion mechanisms including vertical hyperviscosity and anti-aliasing filters.

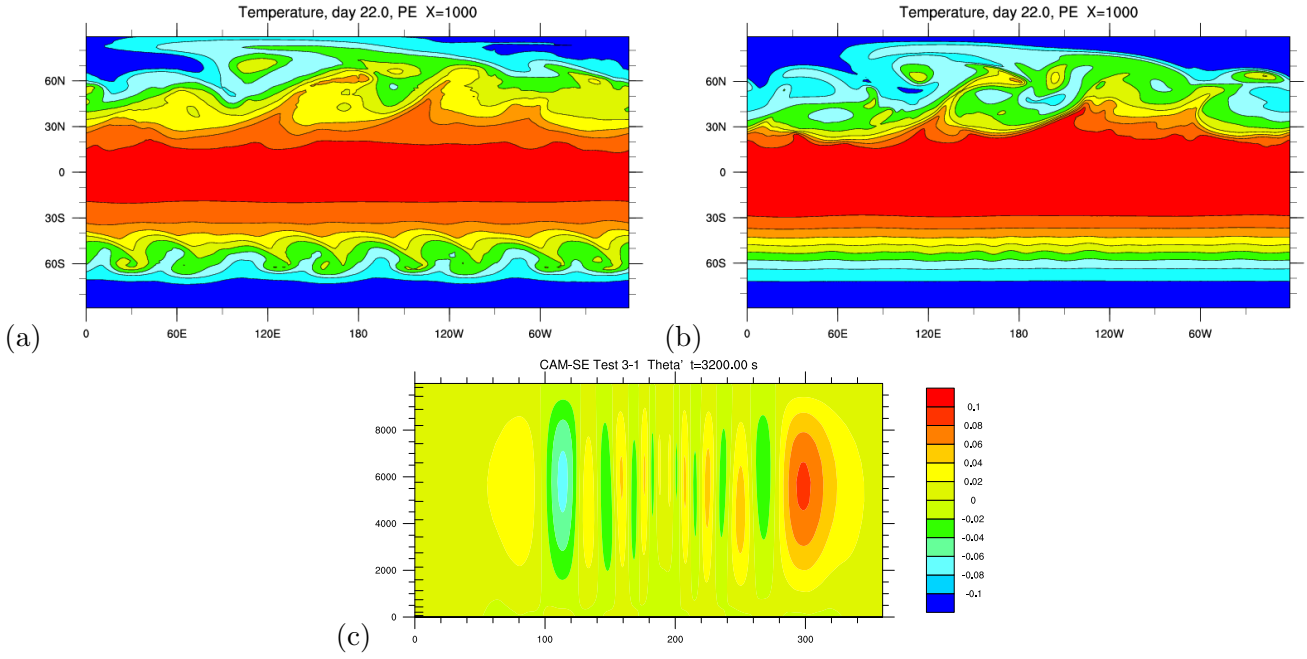

Figure 10: Results of the multi-model framework in HOMME: Employing a spectral vertical representation produces higher accuracy on several DCMIP test with respect to the default CAM-SE solver. (a) DCMIP 4-1 temperature field for the CAM-SE solver. (b) DCMIP 4-1 Temperature field for the PE-SP solver. (c) The NH-SP2 nonhydrostatic model produces greatly improved results on the DCMIP 3-1 orographic wave test.

The best results to date were produced by the vertically-spectral primitive-equation (PE-SP) model and the vertically-spectral compressible Euler model with prognostic potential temperature (NH-SP2). The PE-SP model was constructed merely to validate the spectral vertical operators, to ensure that the results were at least as accurate as the default CAM-SE solver. Surprisingly, the PE-SP model exhibits superior accuracy at the same resolution as can be seen in Fig.10. On DCMIP test 4-1 in particular, the PE-SP model

exhibits smoother contours, greater detail and a delayed onset of instability in the southern hemisphere, which is indicative of reduced numerical error. The NH-SP2 nonhydrostatic model also shows improved accuracy and stability relative to the original finite-difference Laprise formulation. In particular, pressure abnormalities have been eliminated and the results of the DCMIP 3-1 are identical to those produced by other nonhydrostatic model such as ICON-IAP. Improved orographic boundary conditions were implemented as well, testing of which is ongoing.

References

[1] René Laprise. The euler equations of motion with hydrostatic pressure as an independent variable. *Monthly Weather Review*, 120(1):197–207, 2013/04/15 1992.

[2] Paul Aaron Ullrich, Christiane Jablonowski, James Kent, Peter Hjort Lauritzen, Ramachandran D Nair, and Mark A Taylor. Dynamical core model intercomparison project (dcmip) test case document. *DCMIP Summer School*, 2012.

[3] J Thuburn and TJ Woollings. Vertical discretizations for compressible euler equation atmospheric models giving optimal representation of normal modes. *Journal of Computational Physics*, 203(2):386–404, 2005.

[4] Michael D Toy. *Design of a nonhydrostatic atmospheric model based on a generalized vertical coordinate*. ProQuest, 2008.

[5] Francis X Giraldo and M Restelli. A study of spectral element and discontinuous galerkin methods for the navier–stokes equations in nonhydrostatic mesoscale atmospheric modeling: Equation sets and test cases. *Journal of Computational Physics*, 227(8):3849–3877, 2008.

[6] Tzvi Gal-Chen and Richard CJ Somerville. On the use of a coordinate transformation for the solution of the navier-stokes equations. *Journal of Computational Physics*, 17(2):209–228, 1975.

[7] William C Skamarock and Joseph B Klemp. Efficiency and accuracy of the klemp-wilhelmson time-splitting technique. *Monthly Weather Review*, 122(11):2623–2630, 1994.

[8] JM Straka, Robert B Wilhelmson, Louis J Wicker, John R Anderson, and Kelvin K Droegemeier. Numerical solutions of a non-linear density current: A benchmark solution and comparisons. *International Journal for Numerical Methods in Fluids*, 17(1):1–22, 1993.

[9] Roger Alexander. Diagonally implicit runge-kutta methods for stiff ode's. *SIAM Journal on Numerical Analysis*, 14(6):1006–1021, 1977.

[10] Dana A Knoll and David E Keyes. Jacobian-free newton–krylov methods: a survey of approaches and applications. *Journal of Computational Physics*, 193(2):357–397, 2004.

[11] Almut Gassmann. A global hexagonal c-grid non-hydrostatic dynamical core (icon-iap) designed for energetic consistency. *Quarterly Journal of the Royal Meteorological Society*, 139(670):152–175, 2013.

[12] Thomas Allen. Endgame-the met office's next dynamical core. In *The 2010 Workshop on the Solution of Partial Differential Equations on the Sphere*, page 21, 2010.

[13] P Bénard, J Vivoda, J Mašek, P Smolíková, K Yessad, Ch Smith, R Brožková, and J-F Geleyn. Dynamical kernel of the aladin–nh spectral limited-area model: Revised formulation and sensitivity experiments. *Quarterly Journal of the Royal Meteorological Society*, 136(646):155–169, 2010.